Eocene Neo-Tethyan slab breakoff constrained by 45 Ma OIB-type magmatism in southern Tibet

Wei-Qiang Ji[1,2], Fu-Yuan Wu[1,2], Sun-Lin Chung[3,4], Xuan-Ce Wang[5], Chuan-Zhou Liu[1,2], Qiu-Li Li[1], Zhi-Chao Liu[1], Xiao-Chi Liu[1], and Jian-Gang Wang[1]

[1]State Key Laboratory of Lithospheric Evolution, Institute of Geology and Geophysics, Chinese Academy of Sciences, P.O. Box 9825, Beijing 100029, China

[2]CAS Center for Excellence in Tibetan Plateau Earth Sciences, Beijing 100101, China

[3]Institute of Earth Sciences, Academia Sinica, Taipei 11529

[4]Department of Geosciences, National Taiwan University, Taipei 10617

[5]The Institute for Geoscience Research (TIGeR), Department of Applied Geology, Curtin University, Perth, WA 6102, Australia

ABSTRACT

Slab breakoff is one of the primary processes in the evolution of many collisional orogens. In the Tibet–Himalaya Orogen, the timing of breakoff of the Neo-Tethyan slab remains controversial because of a scarcity of solid evidence. This study reports the discovery of Eocene gabbros, dated at 45.0 ± 1.4 Ma (in-situ U–Pb age of titanite) using secondary ion mass spectrometry (SIMS), from the eastern segment of Tethyan Himalaya (TH) in southern Tibet. These rocks show geochemical characteristics similar to those of HIMU-type oceanic island basalt (OIB) and have depleted Sr–Nd isotopes [$^{87}Sr/^{86}Sr(t)$ = 0.70312–0.70317; $\varepsilon_{Nd}(t)$ = +4.9 to +5.0]. It is suggested that the gabbros stand as the first direct evidence for partial melting of the asthenosphere, followed by rapid magma ascent with negligible crustal contamination. This event, combined with relevant studies along

the Indus–Yarlung suture zone, is best explained by a sudden and full-scale detachment of subducted Neo-Tethyan slab at great depth. The breakoff model may account for coeval tectonomagmatic activities (development of small-scale, short-lived magmatism and subsequent termination of the Gangdese arc magmatism) in southern Tibet, and for the abrupt slowdown (ca. 45 Ma) of Indo-Asia convergence.

INTRODUCTION

The formation and evolution of the Tibet–Himalaya Orogen is of great importance to our understanding of collisional orogenesis and related processes (Yin and Harrison, 2000). However, the timing of breakoff of the Neo-Tethyan slab after Indo-Asia collision, which is one of principal steps in the evolution of many collisional orogens, remains enigmatic due to a paucity of relevant evidence. Since slab breakoff may induce coeval magmatism, metamorphism, and other tectonic phenomena (Davies and von Blanckenburg, 1995), the timing can be constrained by studying these aspects of the orogen.

The slab breakoff model has been widely applied in explaining the early Cenozoic geological evolution of southern Tibet. Guillot et al. (1997) tentatively proposed a slab breakoff hypothesis to explain temperature increases during the retrogressive evolution of the Tso Morari eclogites in the NW Himalaya. Subsequently, the detached oceanic slab was identified through tomographic imaging (Van der Voo et al., 1999). Based on a tomography study in the Hindu Kush region, Negredo et al. (2007) inferred that breakoff occurred at ca. 44–48 Ma. Based on the ages of ultra-high pressure (UHP) rocks from the western Himalaya (45–55 Ma) and related geological data, Kohn and Parkinson (2002) argued for slab breakoff at ca. 45 Ma. However, the above-mentioned studies were mainly confined to NW Himalaya, so the timing for slab breakoff in other places along the Indus–Yarlung Suture Zone (IYSZ, >2500 km) needs further researches.

Currently, magmatism associated with breakoff of the Neo-Tethyan slab shows large age range of 69–40 Ma. To the south of the IYSZ that represented a passive continental margin during northward subduction of the Neo-Tethys, middle Eocene (46–42 Ma) anatectic magmatism (Fig. 1A) has been attributed to breakoff of the Neo-Tethyan slab (Hou et al., 2012; Pullen et al., 2011; Zeng et al., 2011). As the thermal perturbation induced by breakoff may have been prolonged, these crust-derived rocks indicate the minimum age of breakoff. On the Lhasa side of the orogen (i.e., the previous active continental margin), various magmatic pulses have been interpreted as indicating slab breakoff, including the early Cenozoic Linzizong volcanic rocks (ca. 69–40 Ma) (Yin and Harrison, 2000), the magmatic peak at ca. 50 Ma (Lee et al., 2009; Zhu et al., 2015), and the termination of Gangdese arc magmatism (45–40 Ma) (Chung et al., 2005). Nevertheless, it is difficult to discriminate between persistent Neo-Tethyan subduction and slab breakoff in terms of the likely genetic mechanism. Moreover, if the detachment depth is greater than the bottom of overriding lithosphere, the thermal perturbation is negligible (van de Zedde and Wortel, 2001). Because the detachment depth is proportional to subduction velocity (Davies and von Blanckenburg, 1995), the extremely high rate of convergence between India and Asia in the early Cenozoic (~14–16 cm/yr from 65 to 50 Ma; van Hinsbergen et al., 2011) should have led to a deep breakoff, producing a weak thermal perturbation in the overlying lithosphere. Therefore, a magmatic pulse in southern Tibet could be ambiguous in terms of constraining the slab breakoff. In the Gaoligong Orogen (No. 6 in Fig. 1A), Xu et al. (2008) proposed that mafic dykes (~42 Ma) with an intraplate affinity represent asthenosphere-derived melts following breakoff. However, no similar magmatism in early Tertiary is recorded inside the plateau.

In this study, we report the first identification of middle Eocene (ca. 45 Ma) oceanic island basalt (OIB) type gabbros from Gyangze region, which intrude the eastern Tethyan Himalaya (TH) (Fig. 1). It is suggested that these rocks formed by partial melting of upwelling asthenosphere as a direct response to breakoff of the Neo-Tethyan slab at ca. 45 Ma.

BACKGROUND AND SAMPLES

The Tibetan Plateau was formed by a series of terrane accretion events, with the last occurring along the IYSZ between the Lhasa terrane to the north and the Himalayas to the south (Yin and Harrison, 2000) (Fig. 1A). Post-collisional magmatism occurred along both sides of the IYSZ, providing an important constraint on the formation and evolution of the plateau (Chung et al., 2005; Wu et al., 2015). The Lhasa terrane contains widespread volcanic and intrusive rocks along its southern margin, which were associated with northward subduction of Neo-Tethyan oceanic lithosphere and subsequent continental collision. There were two main stages of magmatism: an early Tertiary stage represented by the Linzizong volcanic rocks and coeval Gangdese batholith, and an Oligocene–Miocene stage that produced calc-alkaline and potassic–ultrapotassic rocks (Chung et al., 2005). The Himalayas comprises three main units: the TH, High Himalaya (HH), and Lesser Himalaya (LH), separated by the South Tibet Detachment System (STDS) and the Main Central Thrust (MCT) (Fig. 1A). Cenozoic magmatism in the Himalayas consists mainly of Oligocene–Miocene leucogranites that occur in two subparallel belts in the TH and HH (Wu et al., 2015), along with minor middle Eocene (46–42 Ma) granites in the TH (Figs. 1 and 2).

The Langshan gabbros are located to the northeast of Gyangze, in the eastern TH (area C in Fig. 1). These rocks intrude the Late Cretaceous to early Tertiary Zongzhuo Formation, which consists mainly of sandstone, siltstone, and shale. Xenoliths of the Zongzhuo Formation occur in the Langshan gabbros (Fig. DR1B). They show a large variation in grain size from aphanitic near the margin of the intrusion (Fig. DR1C) to coarse-grained in the central part (Fig. DR1F). Six samples collected from different parts of the intrusion (Fig. 1C) were selected for this study. Sample 12FW58 (fine-grained, Fig. DR1D) was collected from the margin, whereas the other samples were collected from inner parts of the intrusion. The Langshan gabbros consist mainly of clinopyroxene and plagioclase (Figs. DR1G and H), with accessory titanite, apatite and Fe-Ti oxides. Field and microscopic observations indicate that the rocks underwent various degrees of low-temperature hydrothermal alteration (i.e., epidotization and carbonatization).

GEOCHRONOLOGY AND GEOCHEMISTRY

Back-scattered electron (BSE) images show that most of the titanite grains from Sample 13JT04 are euhedral and homogeneous without inclusions, indicating that they crystallized rapidly from the magma. Forty-nine analyses were conducted on the titanites which show low U concentrations (1.4–25.7 ppm) and a range of Th/U ratios (0.04–3.10) (Table DR1). The scattered data points on the Tera–Wasserburg diagram yield a lower intercept age of 45.0 ± 1.4 Ma (MSWD = 3.6; Fig. 3A). As the rock textures indicate shallow intrusion and rapid crystallization, the titanite U–Pb age is interpreted as the age of intrusion and crystallization of the magma.

The analyzed samples contain 46.22–49.55 wt.% SiO_2, 4.31–10.38 wt.% MgO with Mg# [100 × molar Mg/(Mg + Fe)] of 42–61, and high TiO_2 (3.08–3.89 wt.%) contents (Table DR2). On the Nb/Y versus Zr/TiO_2 diagram (Fig. DR3), all the samples plot in the field of alkali basalt, reflecting silica-undersaturation. They exhibit trace element distributions similar to those of OIB on a primitive-mantle-normalized spidergram (Fig. 3A). Specifically, they are similar to HIMU basalt, characterized by enrichment in high field strength elements (HFSE) Nb and Ta relative to large ion lithophile elements (LILE, e.g. Th and U) and light rare earth elements (LREE). Their high ratios of U/Pb (0.38–0.56) and Nb/La (1.56–2.12), and low ratios of Th/U (3.87–4.30) and Ba/Nb (6.0–6.4), are also similar to HIMU basalts, which distinguish them from enriched mantle (EM) basalts (Willbold and Stracke, 2006). Since these samples experienced hydrothermal alteration, the apatite Sr–Nd isotopes (Tables DR3 and DR4) were used to trace magma initial isotopic compositions, which reflect depleted source characteristics [$^{87}Sr/^{86}Sr(t)$: 0.70312–0.70317; $\varepsilon_{Nd}(t)$: 4.9–5.0]. The partial melting conditions are estimated to have been P ≈2.4 GPa, T ≈1380 °C, and T_p ≈1400 °C (see details in the Data Repository). The melting pressure corresponds to around 80 km depth, which indicates a shallow garnet-facies mantle source.

EVALUATION OF CRUSTAL CONTAMINATION

Because the Langshan gabbros intruded the TH, it is possible that contamination by continental crust occurred during magma ascent and intrusion. As shown in Figure 3A, the trace element characteristics of continental crust are in sharp contrast with those of OIB, especially for Nb and Pb. Thus, the related trace element ratios of similarly incompatible pairs, such as Nb/U and Pb/Nd, can be sensitive indicators of crustal contamination (Hofmann, 2014). Furthermore, the TH rocks show more enriched isotopes (Liu et al., 2014) than the Langshan gabbros. Crustal contamination should drive the magma composition toward that of continental crust; however, no such trend was identified (Fig. DR4), indicating that crustal contamination is negligible in the Langshan gabbros. This view is supported by the uniform ratios of Nb/U (42–66) and Pb/Nd (10.5–18.5), which are similar to OIB values (Fig. 3B). In addition, the Nb/U ratios are equivalent to the mean of 'non-EM-type' OIB (52 ± 15, Hofmann, 2014).

MAGMA SOURCE AND PETROGENESIS

The Langshan gabbros exhibit OIB-like trace element characteristics and depleted Sr–Nd isotopic compositions. The alkaline OIB characteristics require the presence of enriched components in the mantle source, either from recycled oceanic crust with various continental materials (Hofmann, 2014; Willbold and Stracke, 2006) or from metasomatic processes (for a review, see Niu et al., 2012). The local subcontinental lithospheric mantle belonged to the former Indian passive continental margin, which was poor in metasomatic fluids, as indicated by the absence of post-collisional potassic–ultrapotassic rocks in the region south of the IYSZ (Chung et al., 2005). Moreover, the Himalayan basement has ancient isotopic compositions (cf. Zeng et al., 2011). Thus, the Langshan gabbros could not have been derived from local lithospheric mantle.

If they were derived from the asthenosphere, partial melting may have occurred by increasing temperature or decreasing pressure (McKenzie and Bickle, 1988). The former is commonly associated with the development of mantle plumes; however, there is no evidence for a coeval plume. In addition, the mantle plume model does not account for the E–W-trending zonal distribution of magmatism. Alternatively, decreasing pressure can be achieved by mantle upwelling. After initial continental collision, the upwelling of asthenosphere can be triggered by removal of the thickened lithospheric mantle by delamination or convective thinning, or by breakoff of subducted Neo-Tethyan slab. The small-scale and short-term nature of middle Eocene magmatism is in stark contrast to the characteristics of delamination (large-scale) and/or convective thinning (long-lasting) (Xu et al., 2008). Thus, the favored mechanism for middle Eocene magmatism along the IYSZ is slab breakoff involving Neo-Tethyan oceanic lithosphere (Fig. 4).

In the case of a rapid convergence between India and Asia, slab breakoff would have occurred at great depth (Davies and von Blanckenburg, 1995). For example, it has been estimated that breakoff occurred at least as deep as 120 km, as constrained by the peak metamorphic pressure of continental UHP rocks (Guillot et al., 2008, and references therein), or even deeper if the Indian lithosphere was able to subduct to 200–250 km depth (Chemenda et al., 2000). The compositions of slab-derived components are distinct from different depths. At depths of <80–100 km, subducted oceanic crust releases hydrous fluids that are rich in LILE and LREE, but poor in HFSE (e.g. Nb, Ta and Ti). At greater depths (>150 km), partial melts from oceanic crust are enriched in HFSE due to previous removal of fluid-mobile elements and decomposition of rutile (which controls Nb, Ta, and Ti) (Ringwood, 1990; Willbold and Stracke, 2006, and references therein). The upwelling asthenosphere, infiltrated by HFSE-rich melts, would produce HIMU-like basalts if no obvious continental crust material was incorporated. The formation process of the magma source is similar to that of HIMU basalts from the Cook–Austral Islands (Hanyu et al., 2011). After slab breakoff, these asthenosphere-derived melts intruded the

TH following the rapid exhumation of crustal rocks, resulting in the emplacement of the Langshan intrusion. A high migration rate is needed to explain the absence of obvious crustal contamination characterized by incompatible elements and isotopes (Fig. DR4).

GEOLOGIC IMPLICATIONS

The generation of the Langshan gabbros at Gyangze supports slab breakoff at ca. 45 Ma in the eastern Himalaya, coeval with that in the northwestern Himalaya (Kohn and Parkinson, 2002), indicating that breakoff of the Neo-Tethyan slab was almost synchronous along the whole length of the IYSZ (>2500 km). This is supported by the coeval development of granites (46–42 Ma) along the IYSZ (Fig. 1), reflecting a breakoff-related thermal perturbation along the breakoff window. Rapid breakoff has also been inferred from the constant depth of the slab anomaly on seismic tomographic images (Negredo et al., 2007).

A recent study found that rapid breakoff can slow the rate of slab subduction (Bercovici et al., 2015). Cenozoic convergence between India and Asia shows two clear decelerations, at 52–50 Ma (from 14 to 16 to 8–10 cm/yr) and at ca. 45 Ma (from 8 to 10 to 4–6 cm/yr), after which it maintained a nearly constant rate (4–6 cm/yr) (Patriat and Achache, 1984; van Hinsbergen et al., 2011). While the first deceleration is generally attributed to Indo-Asia collision, the cause of the second is debated (Patriat and Achache, 1984; van Hinsbergen et al., 2011). Based on the present results, it is concluded that the second deceleration was related to a loss of slab pull due to slab breakoff at ca. 45 Ma (Bercovici et al., 2015).

After slab breakoff, subduction would have switched to a mode of high horizontal compression, especially in the Himalayan region (Chemenda et al., 2000). Large-scale crustal shortening across the Himalayas would have resulted in folding and thrusting. However, additional shortening, apart from that estimated from balanced cross-sections, is required to explain paleomagnetic data, such as thrusting along the MCT (Yi et al., 2011). The growth of garnet (from ca. 45 Ma) at the base of the HH in the central segment indicates early movement along the MCT, accompanied by the initiation of prograde metamorphism (Carosi et al., 2014, and references therein). The consistent ages imply that all of these geologic processes are related to slab breakoff, which impeded further continental subduction and induced strong north–south compression. Furthermore, the subducted continental lithosphere rotated upwards to come against the base of the overriding plate after slab breakoff, followed by horizontal subduction of the lithosphere (Chemenda et al., 2000). This process would have driven away the asthenosphere from beneath the Lhasa terrane, and then shielded it from the convective heat, which would have lead to the cessation of Gangdese arc magmatism (45–40 Ma, Fig. 2B).

ACKNOWLEDGMENTS

We thank Georgia Pe-Piper, René Maury, Sally A. Gibson and two others for constructive comments, Editor J. Brendan Murphy for handling, Di-Cheng Zhu for useful suggestion, and Yue-Heng Yang and Chao-Feng Li for help with isotopic analyses. This study was supported by the National Natural Science Foundation of China (grants 41130313, 41572055 and 41222023) and the Australian Research Council (ARC) Future Fellowship (FT140100826) to Xuan-Ce Wang.

REFERENCES CITED

Aikman, A.B., Harrison, T.M., and Lin, D., 2008, Evidence for early (> 44 Ma) Himalayan crustal thickening, Tethyan Himalaya, southeastern Tibet: Earth and Planetary Science Letters, v. 274, p. 14–23, doi:10.1016/j.epsl.2008.06.038.

Bercovici, D., Schubert, G., and Ricard, Y., 2015, Abrupt tectonics and rapid slab detachment with grain damage: Proceedings of the National Academy of Sciences of the United States of America, v. 112, p. 1287–1291, doi:10.1073/pnas.1415473112.

Carosi, R., Montomoli, C., Langone, A., Turina, A., Cesare, B., Iaccarino, S., Fascioli, L., Visonà, D., Ronchi, A., and Rai, S.M., 2014, Eocene partial melting recorded in peritectic garnets from kyanite-gneiss, Greater Himalayan Sequence, central Nepal, *in* Mukherjie, S., et al., eds., Tectonics of the Himalaya: Geological Society, London, Special Publication 412, p. 111–129 doi:10.1144/SP412.1.

Chemenda, A.I., Burg, J.P., and Mattauer, M., 2000, Evolutionary model of the Himalaya-Tibet system: Geopoem based on new modelling, geological and geophysical data: Earth and Planetary Science Letters, v. 174, p. 397–409, doi:10.1016/S0012-821X(99)00277-0.

Chung, S.L., Chu, M.F., Zhang, Y.Q., Xie, Y.W., Lo, C.H., Lee, T.Y., Lan, C.Y., Li, X.H., Zhang, Q., and Wang, Y.Z., 2005, Tibetan tectonic evolution inferred from spatial and temporal variations in post-collisional magmatism: Earth-Science Reviews, v. 68, p. 173–196, doi:10.1016/j.earscirev.2004.05.001.

Davies, J.H., and von Blanckenburg, F., 1995, Slab breakoff: A model of lithosphere detachment and its test in the magmatism and deformation of collisional orogens: Earth and Planetary Science Letters, v. 129, p. 85–102, doi:10.1016/0012-821X(94)00237-S.

Ding, L., Kapp, P., and Wan, X.Q., 2005, Paleocene-Eocene record of ophiolite obduction and initial India-Asia collision, south central Tibet: Tectonics, v. 24, TC3001, doi:10.1029/2004TC001729.

Guillot, S., De Sigoyer, J., Lardeaux, J., and Mascle, G., 1997, Eclogitic metasediments from the Tso Morari area (Ladakh, Himalaya): Evidence for continental subduction during India-Asia convergence: Contributions to Mineralogy and Petrology, v. 128, p. 197–212, doi:10.1007/s004100050303.

Guillot, S., Maheo, G., de Sigoyer, J., Hattori, K.H., and Pecher, A., 2008, Tethyan and Indian subduction viewed from the Himalayan high- to ultrahigh-pressure metamorphic rocks: Tectonophysics, v. 451, p. 225–241, doi:10.1016/j.tecto.2007.11.059.

Hanyu, T., Tatsumi, Y., Senda, R., Miyazaki, T., Chang, Q., Hirahara, Y., Takahashi, T., Kawabata, H., Suzuki, K., and Kimura, J.I., 2011, Geochemical characteristics and origin of the HIMU reservoir: A possible mantle plume source in the lower mantle: Geochemistry, Geophysics, Geosystems, v. 12, Q0AC09.

Hofmann, A.W., 2014, 3.3 - Sampling Mantle Heterogeneity through Oceanic Basalts: Isotopes and Trace Elements, *in* Turekian, H.D.H.K., ed., Treatise on Geochemistry (Second Edition): Oxford, Elsevier, p. 67–101, doi:10.1016/B978-0-08-095975-7.00203-5.

Hou, Z.Q., Zheng, Y.C., Zeng, L.S., Gao, L.E., Huang, K.X., Li, W., Li, Q.Y., Fu, Q., Liang, W., and Sun, Q.Z., 2012, Eocene-Oligocene granitoids in southern Tibet: Constraints on crustal anatexis and tectonic evolution of the Himalayan orogen:

Earth and Planetary Science Letters, v. 349–350, p. 38–52, doi:10.1016/j.epsl.2012.06.030.

Ji, W.Q., Wu, F.Y., Chung, S.L., and Liu, C.Z., 2014, The Gangdese magmatic constraints on a latest Cretaceous lithospheric delamination of the Lhasa terrane, southern Tibet: Lithos, v. 210–211, p. 168–180, doi:10.1016/j.lithos.2014.10.001.

Kohn, M.J., and Parkinson, C.D., 2002, Petrologic case for Eocene slab breakoff during the Indo-Asian collision: Geology, v. 30, p. 591–594, doi:10.1130/0091-7613(2002)030<0591:PCFESB>2.0.CO;2.

Lee, H.Y., Chung, S.L., Lo, C.H., Ji, J.Q., Lee, T.Y., Qian, Q., and Zhang, Q., 2009, Eocene Neotethyan slab breakoff in southern Tibet inferred from the Linzizong volcanic record: Tectonophysics, v. 477, p. 20–35, doi:10.1016/j.tecto.2009.02.031.

Liu, Z.C., Wu, F.Y., Ji, W.Q., Wang, J.G., and Liu, C.Z., 2014, Petrogenesis of the Ramba leucogranite in the Tethyan Himalaya and constraints on the channel flow model: Lithos, v. 208–209, p. 118–136, doi:10.1016/j.lithos.2014.08.022.

McKenzie, D., and Bickle, M.J., 1988, The volume and composition of melt generated by extension of the lithosphere: Journal of Petrology, v. 29, p. 625–679, doi:10.1093/petrology/29.3.625.

Negredo, A.M., Replumaz, A., Villaseñor, A., and Guillot, S., 2007, Modeling the evolution of continental subduction processes in the Pamir-Hindu Kush region: Earth and Planetary Science Letters, v. 259, p. 212–225, doi:10.1016/j.epsl.2007.04.043.

Niu, Y., Wilson, M., Humphreys, E.R., and O’Hara, M.J., 2012, A trace element perspective on the source of ocean island basalts (OIB) and fate of subducted ocean crust (SOC) and mantle lithosphere (SML): Episodes, v. 35, p. 310–327.

Patriat, P., and Achache, J., 1984, India-Eurasia collision chronology has implications for crustal shortening and driving mechanism of plates: Nature, v. 311, p. 615–621, doi:10.1038/311615a0.

Pullen, A., Kapp, P., DeCelles, P.G., Gehrels, G.E., and Ding, L., 2011, Cenozoic anatexis and exhumation of Tethyan Sequence rocks in the Xiao Curia Range, Southwest Tibet: Tectonophysics, v. 501, p. 28–40, doi:10.1016/j.tecto.2011.01.008.

Ringwood, A., 1990, Slab-mantle interactions: 3. Petrogenesis of intraplate magmas and structure of the upper mantle: Chemical Geology, v. 82, p. 187–207, doi:10.1016/0009-2541(90)90081-H.

Rudnick, R., and Gao, S., 2003, Composition of the Continental Crust, *in* Holland, H.D. and Turekian, K.K., eds., Treatise on Geochemistry, Volume 3: New York, Elsevier, p. 1–64, doi:10.1016/B0-08-043751-6/03016-4.

Sun, S.-S., and McDonough, W.F., 1989, Chemical and isotopic systematics of oceanic basalts: Implications for mantle composition and processes, *in* Saunders, A.D., and Norry, M.J., eds., Magmatism in the ocean basins: Geological Society, London, Special Publication 42, p. 313–345, doi:10.1144/GSL.SP.1989.042.01.19.

van de Zedde, D.M.A., and Wortel, M.J.R., 2001, Shallow slab detachment as a transient source of heat at midlithospheric depths: Tectonics, v. 20, p. 868–882, doi:10.1029/2001TC900018.

Van der Voo, R., Spakman, W., and Bijwaard, H., 1999, Tethyan subducted slabs under India: Earth and Planetary Science Letters, v. 171, p. 7–20, doi:10.1016/S0012-821X(99)00131-4.

van Hinsbergen, D.J.J., Steinberger, B., Doubrovine, P.V., and Gassmoeller, R., 2011, Acceleration and deceleration of India-Asia convergence since the Cretaceous: Roles of mantle plumes and continental collision: Journal of Geophysical Research. Solid Earth, v. 116, p. B06101.

Willbold, M., and Stracke, A., 2006, Trace element composition of mantle end-members: Implications for recycling of oceanic and upper and lower continental crust: Geochemistry Geophysics Geosystems, v. 7, Q04004, doi:10.1029/2005GC001005.

Wu, F.Y., Liu, Z.C., Liu, Z.C., and Ji, W.Q., 2015, Himalayan leucogranite: Petrogenesis and implications to orogenesis and plateau uplift: Acta Petrologica Sinica, v. 31, p. 1–36.

Xu, Y.G., Lan, J.B., Yang, Q.J., Huang, X.L., and Qiu, H.N., 2008, Eocene break-off of the Neo-Tethyan slab as inferred from intraplate-type mafic dykes in the Gaoligong orogenic belt, eastern Tibet: Chemical Geology, v. 255, p. 439–453, doi:10.1016/j.chemgeo.2008.07.016.

Yi, Z., Huang, B., Chen, J., Chen, L., and Wang, H., 2011, Paleomagnetism of early Paleogene marine sediments in southern Tibet, China: Implications to onset of the India–Asia collision and size of Greater India: Earth and Planetary Science Letters, v. 309, p. 153–165.

Yin, A., and Harrison, T.M., 2000, Geologic evolution of the Himalayan-Tibetan orogen: Annual Review of Earth and Planetary Sciences, v. 28, p. 211–280, doi:10.1146/annurev.earth.28.1.211.

Zeng, L.S., Gao, L.E., Xie, K.J., and Jing, L.Z., 2011, Mid-Eocene high Sr/Y granites in the Northern Himalayan Gneiss Domes: Melting thickened lower continental crust:

Earth and Planetary Science Letters, v. 303, p. 251–266, doi:10.1016/j.epsl.2011.01.005.

Zhu, D.C., Wang, Q., Zhao, Z.D., Chung, S.L., Cawood, P.A., Niu, Y., Liu, S.A., Wu, F.Y., and Mo, X.X., 2015, Magmatic record of India-Asia collision: Scientific Reports, v. 5, p. 14289, doi:10.1038/srep14289.

FIGURE CAPTIONS

Figure 1. A: Location of the study region (labeled “B”) on the Tibet Plateau. B: Geological map of the study region. C: Outcrops of gabbros near Langshan (The base map is from Google Earth). The numbers in circle denote the locations of middle Eocene magmatism: 1. Xiao Gurla Range (Pullen et al., 2011); 2. Niuku (Ding et al., 2005); 3. Ramba (Liu et al., 2014); 4. Hawong (our unpublished data); 5. Yalaxiangbo-Quedang-Dala (Aikman et al., 2008; Hou et al., 2012; Zeng et al., 2011); 6. Gaoligong (Xu et al., 2008); and NW Himalaya UHP rocks: 7. Tso Morari; 8. Kaghan Valley.

Figure 2. A: Tera–Wasserburg diagram showing the results of titanite U–Pb dating for Sample 13JT04. B: Probability plot of the ages of Cenozoic magmatism in southern Tibet. Data for TH granite, Gangdese batholith and Linzizong volcanics are from Wu et al. (2015), Ji et al. (2012) and Lee et al. (2009), respectively, and references therein.

Figure 3. A: Primitive-mantle-normalized spidergram for the Langshan gabbros. B: Plot of Nb/U versus Nd/Pb. Normalizing values are from Sun and McDonough (1989). The

data for OIB and N-MORB, and CC (bulk continental crust) are from Sun and McDonough (1989) and Rudnick and Gao (2003), respectively.

Figure 4. Schematic illustration for an abrupt and full-scale detachment (ca. 45 Ma) of subducted Neo-Tethyan slab at great depth for coeval development of several records in southern Tibet, including slowdown of convergence rate between India and Asia, the youngest UHP rocks from NW Himalaya, HIMU OIB-type Langshan gabbros, small-scale, short-lived magmatism along IYSZ, and subsequent cessation of Gangdese arc magmatism.

[1]GSA Data Repository item 2016xxx, analytical methods, estimation of primitive component and partial melting conditions, evaluation of alteration, Tables DR1–DR4 and Figures DR1–DR4, is available online at www.geosociety.org/pubs/ft2016.htm, or on request from editing@geosociety.org or Documents Secretary, GSA, P.O. Box 9140, Boulder, CO 80831, USA.

Figure 1

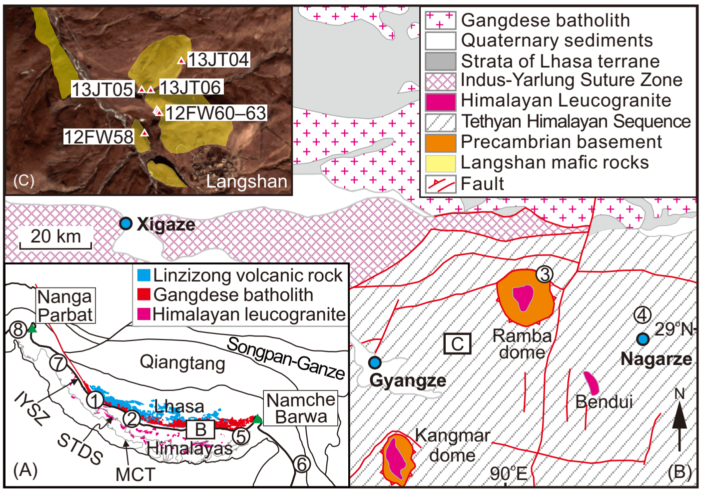

Gangdese batholith
Quaternary sediments
Strata of Lhasa terrane
Indus-Yarlung Suture Zone
Himalayan Leucogranite
Tethyan Himalayan Sequence
Precambrian basement
Langshan mafic rocks
Fault
13JT04
13JT05
13JT06
12FW60–63
12FW58
(C)
Langshan
Xigaze
20 km
Linzizong volcanic rock
Gangdese batholith
Himalayan leucogranite
Nanga Parbat
Qiangtang
Songpan-Ganze
Lhasa
Namche Barwa
IYSZ
STDS
MCT
Himalayas
B
(A)
C
Ramba dome
29°N
Nagarze
Gyangze
Bendui
Kangmar dome
90°E
N
(B)

Figure 2

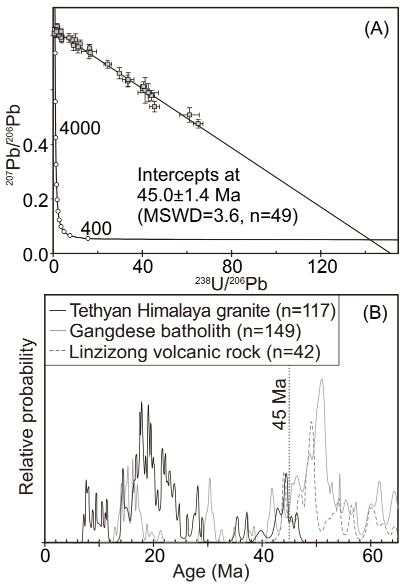

(A)
4000
400
Intercepts at
45.0±1.4 Ma
(MSWD=3.6, n=49)
207Pb/206Pb
238U/206Pb
(B)
Tethyan Himalaya granite (n=117)
Gangdese batholith (n=149)
Linzizong volcanic rock (n=42)
45 Ma
Relative probability
Age (Ma)

Figure 3

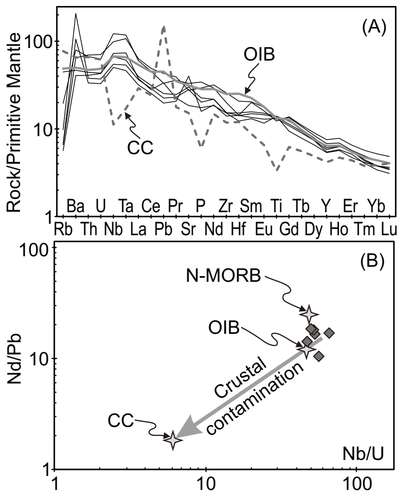

(A)
Rock/Primitive Mantle
100
10
1
OIB
CC
Ba U Ta Ce Pr P Zr Sm Ti Tb Y Er Yb
Rb Th Nb La Pb Sr Nd Hf Eu Gd Dy Ho Tm Lu
(B)
100
10
1
Nd/Pb
N-MORB
OIB
Crustal contamination
CC
Nb/U
1
10
100

Figure 4

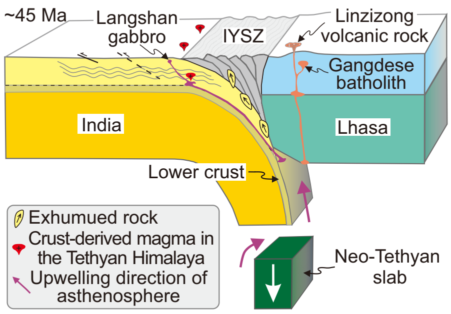

~45 Ma
Langshan gabbro
IYSZ
Linzizong volcanic rock
Gangdese batholith
India
Lhasa
Lower crust
Exhumued rock
Crust-derived magma in the Tethyan Himalaya
Upwelling direction of asthenosphere
Neo-Tethyan slab

Data Depository

METHODS SUMMARY

Analytical methods

Titanite U-Pb dating: Titanite crystals are separated from one coarse grain sample (13JT04). They and titanite U-Pb dating standard (BLR-1, Aleinikoff et al., 2002) were mounted onto the same epoxy resin mounts. Then the epoxy mount were polished to expose a depth of about one half of the crystal. Titanite U-Pb dating was carried out using Cameca IMS-1280 at the Institute of Geology and Geophysics, Chinese Academy of Sciences. Detailed instrumental parameters and analytical procedures are similar to the perovskite SIMS U-Pb dating method (Li et al., 2010) and are the same as the titanite SIMS U-Pb dating method described in Li et al. (2014). During analysis, the ellipsoidal spot was about 20×30 μm in size. BLR-1 was used as standard for titanite U-Pb analysis, and was analyzed twice after every 5 analyses for unknowns. Common Pb correction based on ^{207}Pb was used for individual analysis and an average $^{206}Pb/^{238}U$ age with 2σ or 95% confidence level was calculated using the ISOPLOT 3.0 software (Ludwig, 2003). The dating results are listed in Table DR1 and presented in Fig. 2a. As most dating spots have relative high common Pb contents, we adopted the lower intercept age (45.0 ± 1.4 Ma) on the Tera-Wasserburg U-Pb concordia diagram as the titanite age. And the weighted mean of ^{207}Pb corrected $^{206}Pb/^{238}U$ age (45.2 ± 7.7 Ma, n=49) is equal to the lower intercept age within error.

Whole-rock geochemistry: Whole-rock major elements, trace elements and Sr-Nd isotopes were analyzed in Department of Geosciences, National Taiwan University, following the methods of Lee et al. (2012). Major elements were determined by X-ray fluorescence (XRF) method with analytical uncertainties better than 5% for all elements. Trace elements were measured by inductively coupled plasma mass spectrometry (ICP-MS) method with the analytical accuracy and precision generally better than 3%. The major and trace elements are presented in Table DR2. As all the studied samples have relatively high LOI values, the major element abundances were recalculated to 100% on the basis of volatile-free and the recalculated values were used in data interpretation. Whole-rock Sr-Nd isotopes were analyzed by Multi-Collector Inductively-Coupled plasma Mass Spectrometry (MC-ICPMS), Thermo Electron Finnigan Neptune, at Department of Geosciences, National Taiwan University. The detailed method can be found in Lee et al. (2012). Within Sr and Nd isotopic fractionation were normalized to $^{86}Sr/^{88}Sr$ = 0.1194 and $^{146}Nd/^{144}Nd$ = 0.7129, respectively.

In-situ apatite Sr-Nd isotopes: We only separated apatites from some coarse-grained samples (12FW60, 12FW63 and 13JT04). The apatite crystals were mounted onto epoxy resin mounts. Then the mount was polished to expose a depth of about one third of the apatite crystals. Then in-situ apatite Sr-Nd isotopes were conducted on a Thermo-Finnigan Nepture MC-ICPMS, coupled with a 193 nm ArF Excimer laser ablation system (Geolas plus), at the Institute of Geology and Geophysics, Chinese Academy of Sciences. Detailed instrumental parameters and analytical procedures are described in Yang et al. (2014). The apatite Sr and Nd isotopes are presented in Tables DR3 and DR4, respectively. The measured $^{87}Sr/^{86}Sr$ ratios for apatite standards AP1 and Slyudyanka are 0.71133±0.00004 (n=12) and 0.70769±0.00004 (n=13), respectively, identical to the recommended values (AP1: 0.71136±0.00008; Slyudyanka: 0.70769±0.00015) (Yang et al., 2014).The measured $^{143}Nd/^{144}Nd$ ratios for apatite standards AP2 and UWA-1 are 0.511010±0.000024 (n=14) and 0.512320±0.000020 (n=15), respectively, equal to the recommended values (AP2: 0.511008±0.000042; UWA-1: 0.512304±0.000051) within error (Yang et al., 2014).

Detailed method for estimation of primitive component and partial melting conditions

Primary magma compositions of basaltic rocks can provide constraints on the thermochemical state of their mantle sources (cf. Lee et al., 2009). Among all studied samples, Sample 12FW58 has the highest MgO (10.38 wt.%), Cr (222 ppm) and Ni (172 ppm), but the lowest Al_2O_3 (13.7 wt.%) and alkali contents (Na_2O+K_2O = 3.24 wt.%). This sample also displays a fine-grained texture, suggesting fast crystallization and low degree of mineral cumulation. Therefore, we suggest that this sample more compositionally approximates to the primary magmas of Langshan mafic intrusion, i.e., representing the most primitive component of Langshan gabbros. Therefore, we chose 12FW58 as a starting material to estimate the primary melt composition following the method described in Wang et al. (2012). Because the geochemical characteristics of the Langshan mafic rocks indicate a fertile mantle source, the equilibrium mantle olivine Fo = 90 was used in the following calculation. An important variable in fractionation correction is the proportion of Fe^{3+} relative to Fe^{2+} in the magma. Arc magmas are generally thought to be more oxidized although by how much is still debated. Evidence from direct measurement of olivine-host melt inclusion suggested a more oxidized oxygen fugacity with $Fe^{3+}/\sum Fe$ ratio 0.18−0.32 (Kelley and Cottrell, 2009) and 0.19−0.26 (Brounce et al., 2014). However, recent studies of V/Sc systematics suggest that the mantle source regions of primitive arc magmas may only be slightly more oxidizing (up to 1–2 orders of magnitude greater than the FMQ buffer (Lee et al., 2005) and that the oxidized nature of erupted magmas themselves may be due to self-oxidation imparted by water dissociation during magmatic differentiation or ascent (Holloway, 2004). Variations in $Fe^{3+}/\sum Fe$ can introduce significant differences in estimated compositions of parental liquids, notably Mg#. For instance, increasing $Fe^{3+}/\sum Fe$ from 0.2 to 0.3 would result in increasing of 0.3−0.5 wt.% SiO_2 and 0.6−0.8 wt.% Al_2O_3, but decreasing of ~1.0 wt.% FeO and 1.7−1.9 wt.% MgO in final estimated primary melts. In this study, we choose $Fe^{3+}/\sum Fe$ = 0.2 to estimate the primary melt compositions. The final estimated primary melt compositions for 12FW58 are as follows: SiO_2 = 46.1 wt.%, TiO_2 = 2.8 wt.%, Al_2O_3 = 11.8 wt.%, FeO = 10.0 wt.%, MgO = 16.3 wt.%, CaO = 7.7 wt.%, and Ce = 74 ppm.

H_2O behaviors like a typical incompatible trace elements, such as Ce, during mantle melting and subsequent magma evolution, thus H_2O/Ce ratios have been as an important constraint on the H_2O content of the upper mantle (Dixon et al., 2002; Kelley et al., 2006; Workman et al., 2006; Cooper et al., 2012). The H_2O/Ce ratios measured in arc magmas span nearly two orders of magnitude, from ~300 (Irazu volcano in Costa Rica) to 21,000 (Volcano A in Tonga), and mostly higher than 10000 (Cooper et al., 2012). The Nb-enriched arc basalts were demonstrated to contain low water concentration (Sorbadere et al., 2013), thus the lowest H_2O/Ce of 300 was used to constrain magma water concentration. According to estimated primary Ce concentration (74 ppm) and H_2O/Ce ratio, the water content of primary melt is ≥ 2.2 wt.%. Evidence from the Central American volcanoes showed that primary water concentration are also tightly correlated with Ba/La, as H_2O (at Fo91) = 0.0481 × (Na/La) + 1.1294 (Sadofsky et al., 2008). The primary water concentration is estimated at about 1.64 wt.%, resulting in 1.75 wt.% primary melt water concentration when correction is equilibrated with Fo90.

Based on the recent thermobarometer (Lee et al., 2009), a pressure-temperature condition of 2.6 GPa and 1478 ℃ was estimated for the primary melt of sample 12FW58, comparable with the results (2.5 GPa and 1490 ℃) yielded by the method of Albarède (1992). The estimated primary melt gives a mantle potential temperature (T_p) of 1490 ℃, according to T_p (℃) = 1463 + 12.74 × MgO – 2924/MgO (e.g., Herzberg et al., 2007). It is noteworthy that the calculation did not take into account the effect of water. The estimated minimum water concentration of 2.2−1.75 wt.% would suppress their melt temperatures by 91−98 ℃ from a perfectly anhydrous system using function of deltaT = 74.403 × (H_2O wt.%)$^{0.352}$ (Falloon and Danyushevsky, 2000). The final melting pressure and temperature is corrected by magma H_2O of 1.7 wt.% using thermobarometer proposed by Lee et al. (2009). The finally corrected melting P-T results are followings: P ≈ 2.4 GPa, T ≈ 1380 ℃, and T_p ≈ 1400 ℃.

The calculated melting pressure is similar to that constrained by the fractionated REE patterns (such as $(La/Yb)_{CN}$ = 9.3−14.4, $(Sm/Yb)_{CN}$ = 3.5−4.7 and $(Dy/Yb)_{CN}$ = 1.7−2.2) which suggest that partial melting occurred in the garnet stability field (Willbold and Stracke, 2006), i.e., in a garnet-facies mantle source with depth greater than 80 km (McKenzie and O'Nions, 1991). Together with the estimated pressure, the partial melting depth is of shallow garnet-facies at around 80 km.

Evaluation of alteration

The analyzed samples of Langshan intrusion show high LOI (loss on ignation) values, mainly consisting of H_2O^+ (crystal water from secondary minerals) and CO_2. As the mineral assemblage suggests an anhydrous primary magma, the measured H_2O^+ and CO_2 contents reflect degrees of hydrothermal alteration and carbonatization. Thus, before introducing and discussing the geochemical characteristics of these samples, it is important to consider the likely effect of alteration. The major elements, the highly fluid-mobile elements (Cs, Rb, Ba, Pb, Sr and U) and Sr-Nd isotopes show no correlation with the values of H_2O^+, CO_2 and LOI (Figure DR2) and the distributed patterns of trace element shown by samples of different alteration degrees are very similar (Fig. 3a). Besides, the coherent behavior of fluid-mobile (e.g., Rb, K, U) and fluid-immobile elements (e.g., Th, Nb) can be used as proxy for alteration (Willbold and Stracke, 2006). The uniform ratios (e.g., Th/U = 3.87−4.30 and Nb/U = 42−66) suggest that the samples are not seriously affected by later alteration. Furthermore, their Nb/U ratios (42−66, averaged as 54) are close to the canonical value of oceanic basalts (47 ± 10, Hofmann et al., 1986) and identical to the mean of 'no-EM-type' OIB (52 ± 15, Hofmann, 2014). This indicates that the alteration is relatively insignificant for all the analyzed samples that passed our tests.

Notably, the samples show large variation of Ba (284−1450 ppm), as indicated by the various enrichments of Ba in the spidergram (Fig. 3a). Samples 13JT05 (Ba: 739 ppm) and 13JT06 (Ba: 1450 ppm) have obviously higher concentrations of Ba than other samples (284−556 ppm). However, as they are the freshest on the basis of microscope observations and the lowest LOI contents, they should be least affected by alterations. In other words, the remarkable enrichment of Ba in Samples 13JT05 and 13JT06 relative to the others could not be attributed to alteration. The low Ba samples show relatively large LOI contents (6.21−9.26 wt.%), but their Ba/Nb ratios (6.0−6.4) are uniform and similar to that of HIMU basalts (Willbold and Stracke, 2006). The uniform ratios of other incompatible element pairs also suggest that they should be not significantly affected by alteration (see above and discussion). Consequently, a tentative explanation for variation of Ba is that it may reflect other process in the earlier magma evolution rather than later alteration.

However, the whole-rock Sr-Nd isotopes could be affected by the alteration. The whole-rock Rb/Sr ratios (0.005 to 0.073) and Sr isotopes ($^{87}Sr/^{86}Sr$ = 0.706719−0.707302) exhibit relatively large variations (Fig. DR5), whereas their Sm/Nd ratios (0.21−0.24) and $^{143}Nd/^{144}Nd$ values (0.512878−0.512937) are homogeneous. As these samples underwent various alterations, the variation of Sr isotope would be ascribed to hydrothermal alteration. Thus, we also analyzed in-situ Sr-Nd isotopes for apatites separated from the coarse-grained samples which are big enough for analysis. The apatites are colourless and transparent with good crystal form and few inclusions. The $^{87}Rb/^{86}Sr$ ratios (most < 0.002) of the apatites (Table DR3) are very low, so the apatite $^{87}Sr/^{86}Sr$ ratios for Samples 12FW63 (0.70288−0.70338, mean of 0.70317±0.00006) and 13JT04 (0.70292−0.70339, mean of 0.70312±0.00004) are identical to their initial values ($^{87}Sr/^{86}Sr_{(t)}$). The $^{87}Sr/^{86}Sr_{(t)}$ values of apatites are obviously low than that of the whole-rock (Fig. DR5). The measured apatite $^{143}Nd/^{144}Nd$ ratios for Samples 12FW60 and 12FW63 are 0.51280−0.51295 and 0.51280−0.51298, respectively, with their $\varepsilon_{Nd}(t)$ values of 4.9±0.4 and 5.0±0.4, respectively (Table DR4). As the apatites have not been affected by later alteration, their initial Sr-Nd isotopes most likely represent the primitive isotopic compositions for the magma, which are similar to that of the HIMU OIB rocks from Cook-Austal Islands (Fig. DR5).

References:

Aikman, A.B., Harrison, T.M., and Hermann, J., 2012, The origin of Eo- and Neo-himalayan granitoids, Eastern Tibet: Journal of Asian Earth Sciences, v. 58, p. 143-157.

Albarède, F., 1992, How deep do common basaltic magmas form and differentiate: Journal of Geophysical Research-Solid Earth, v. 97, p. 10997−11009.

Aleinikoff, J.N., Wintsch, R.P., Fanning, C.M., and Dorais, M.J., 2002, U-Pb geochronology of zircon and polygenetic titanite from the Glastonbury Complex, Connecticut, USA: an integrated SEM, EMPA, TIMS, and SHRIMP study: Chemical Geology, v. 188, p. 125–147.

Brounce, M.N., Kelley, K.A., Cottrell, E., 2014. Variations in $Fe^{3+}/\sum Fe$ of Mariana arc basalts and mantle wedge f_{O2}. Journal of Petrology 55, 2513–2536.

Cooper, L. B., Ruscitto, D. M., Plank, T., Wallace, P. J., Syracuse, E. M., and Manning, C. E., 2012, Global variations in H_2O/Ce: 1. Slab surface temperatures beneath volcanic arcs: Geochemistry Geophysics Geosystems, v. 13, no. 3, Q03024.

Dixon, J. E., Leist, L., Langmuir, C., and Schilling, J.-G., 2002, Recycled dehydrated lithosphere observed in plume-influenced mid-ocean-ridge basalt: Nature, v. 420, no. 6914, p. 385–389.

Falloon, T. J., and Danyushevsky, L. V., 2000, Melting of Refractory Mantle at 1.5, 2 and 2.5 GPa under Anhydrous and H2O-undersaturated Conditions: Implications for the Petrogenesis of High-Ca Boninites and the Influence of Subduction Components on Mantle Melting: Journal of Petrology, v. 41, no. 2, p. 257–283.

Hanyu, T., Tatsumi, Y., Senda, R., Miyazaki, T., Chang, Q., Hirahara, Y., Takahashi, T., Kawabata, H., Suzuki, K., and Kimura, J.I., 2011, Geochemical characteristics and origin of the HIMU reservoir: A possible mantle plume source in the lower mantle: Geochemistry, Geophysics, Geosystems, v. 12, Q0AC09.

Herzberg, C., Asimow, P.D., Arndt, N., Niu, Y.L., Lesher, C.M., Fitton, J.G., Cheadle, M.J., and Saunders, A.D., 2007, Temperatures in ambient mantle and plumes: Constraints from basalts, picrites, and komatiites: Geochemistry Geophysics Geosystems, v. 8, Q02006.

Hofmann, A.W., Jochum, K.P., Seufert, M., and White, W.M., 1986, Nb and Pb in oceanic basalts: New constraints on mantle evolution: Earth and Planetary Science Letters, v. 79, p. 33−45.

Hofmann, A. W., 2014, 3.3 - Sampling Mantle Heterogeneity through Oceanic Basalts: Isotopes and Trace Elements, in Turekian, H. D. H. K., ed., Treatise on Geochemistry (Second Edition): Oxford, Elsevier, p. 67-101.

Holloway, J. R., 2004, Redox reactions in seafloor basalts: possible insights into silicic hydrothermal systems: Chemical Geology, v. 210, no. 1–4, p. 225–230.

Hou, Z.Q., Zheng, Y.C., Zeng, L.S., Gao, L.E., Huang, K.X., Li, W., Li, Q.Y., Fu, Q., Liang, W., and Sun, Q.Z., 2012, Eocene-Oligocene granitoids in southern Tibet: Constraints on crustal anatexis and tectonic evolution of the Himalayan orogen: Earth and Planetary Science Letters, v. 349–350, p. 38–52

Jiang, Z., Wang, Q., Wyman, D.A., Shi, X., Yang, J., Ma, L., and Gou, G., 2015, Zircon U–Pb geochronology and geochemistry of Late Cretaceous–early Eocene granodiorites in the southern Gangdese batholith of Tibet: petrogenesis and implications for geodynamics and Cu±Au±Mo mineralization: International Geology Review, v. 57, p. 373-392.

Kelley, K. A., Plank, T., Grove, T. L., Stolper, E. M., Newman, S., and Hauri, E., 2006, Mantle melting as a function of water content beneath back-arc basins: Journal of Geophysical Research, v. 111.

Kelley, K. A., and Cottrell, E., 2009, Water and the oxidation state of subduction zone magmas: Science, v. 325, no. 5940, p. 605–607.

Lee, C.-T. A., Leeman, W. P., Canil, D., and Li, Z.X. A., 2005, Similar V/Sc systematics in MORB and arc basalts: Implications for the oxygen fugacities of their mantle source regions: Journal of Petrology, v. 46, no. 11, p. 2313–2336.

Lee, C.-T.A., Luffi, P., Plank, T., Dalton, H., and Leeman, W.P., 2009, Constraints on the depths and temperatures of basaltic magma generation on Earth and other terrestrial planets using new thermobarometers for mafic magmas: Earth and Planetary Science Letters, v. 279, p. 20−33.

Lee, H.Y., Chung, S.L., Ji, J., Qian, Q., Gallet, S., Lo, C.H., Lee, T.Y., and Zhang, Q., 2012, Geochemical and Sr-Nd isotopic constraints on the genesis of the Cenozoic Linzizong volcanic successions, southern Tibet: Journal of Asian Earth Sciences, v. 53, p. 96–114.

Li, Q.L., Li, X.H., Liu, Y., Wu, F.Y., Yang, J.H., and Mitchell, R.H., 2010, Precise U–Pb and Th–Pb age determination of kimberlitic perovskites by secondary ion mass spectrometry: Chemcal Geology, v. 269, p. 396–405.

Li, Y., Zhou, H.W., Li, Q.L., Xiang, H., Zhong, Z.Q., and Brouwer, F.M., 2014, Palaeozoic polymetamorphism in the North Qinling orogenic belt, Central China: Insights from petrology and in situ titanite and zircon U–Pb geochronology: Journal of Asian Earth Sciences, v. 92, p. 77–91.

Liu, Z.C., Wu, F.Y., Ji, W.Q., Wang, J.G., and Liu, C.Z., 2014, Petrogenesis of the Ramba leucogranite in the Tethyan Himalaya and constraints on the channel flow model: Lithos, v. 208–209, p. 118–136

Ludwig, K.R., 2003, ISOPLOT 3.0: A Geochronological Toolkit for Microsoft Excel: Berkeley Geochronology Center Special Publicaition, California, 70 p.

Ma, L., Wang, B.D., Jiang, Z.Q., Wang, Q., Li, Z.X., Wyman, D.A., Zhao, S.R., Yang, J.H., Gou, G.N., and Guo, H.F., 2014, Petrogenesis of the Early Eocene adakitic rocks in the Napuri area, southern Lhasa: Partial melting of thickened lower crust during slab break-off and implications for crustal thickening in southern Tibet: Lithos, v. 196–197, p. 321-338.

Mahoney, J.J., Frei, R., Tejada, M., Mo, X., Leat, P., and Nägler, T., 1998, Tracing the Indian Ocean mantle domain through time: isotopic results from old West Indian, East Tethyan, and South Pacific seafloor: Journal of Petrology, v. 39, p. 1285-1306.

McKenzie, D., and Onions, R.K., 1991, Partial melt distributions from inversion of rare earth element concentrations: Journal of Petrology, v. 32, p. 1021−1091.

Mo, X., Hou, Z., Niu, Y., Dong, G., Qu, X., Zhao, Z., and Yang, Z., 2007, Mantle contributions to crustal thickening during continental collision: Evidence from Cenozoic igneous rocks in southern Tibet: Lithos, v. 96, p. 225-242.

Mo, X., Niu, Y., Dong, G., Zhao, Z., Hou, Z., Zhou, S., and Ke, S., 2008, Contribution of syncollisional felsic magmatism to continental crust growth: A case study of the Paleogene Linzizong volcanic Succession in southern Tibet: Chemical Geology, v. 250, p. 49-67.

Sadofsky, S., Portnyagin, M., Hoernle, K., and Bogaard, P., 2008, Subduction cycling of volatiles and trace elements through the Central American volcanic arc: evidence from melt inclusions: Contributions to Mineralogy and Petrology, v. 155, no. 4, p. 433–456.

Sorbadere, F., Schiano, P., Métrich, N., and Bertagnini, A., 2013, Small-scale coexistence of island-arc- and enriched-MORB-type basalts in the central Vanuatu arc: Contributions to Mineralogy and Petrology, v. 166, no. 5, p. 1305–1321.

Rudnick, R., and Gao, S., 2003, Composition of the continental crust: Treatise on geochemistry, v. 3, p. 1-64.

Sun, S.-S., and McDonough, W. F., 1989, Chemical and isotopic systematics of oceanic basalts: implications for mantle composition and processes: Geological Society, London, Special Publications, v. 42, no. 1, p. 313-345.

Wang, Q., Zhu, D.C., Cawood, P.A., Zhao, Z.D., Liu, S.A., Chung, S.L., Zhang, L.L., Liu, D., Zheng, Y.C., and Dai, J.G., 2015a, Eocene magmatic processes and crustal thickening in southern Tibet:

Insights from strongly fractionated ca. 43 Ma granites in the western Gangdese Batholith: Lithos, v. 239, p. 128-141.

Wang, R., Richards, J.P., Hou, Z.Q., An, F., and Creaser, R.A., 2015b, Zircon U–Pb age and Sr–Nd–Hf–O isotope geochemistry of the Paleocene–Eocene igneous rocks in western Gangdese: Evidence for the timing of Neo-Tethyan slab breakoff: Lithos, v. 224–225, p. 179-194.

Wang, X.C., Li, Z.X., Li, X.H., Li, J., Liu, Y., Long, W.G., Zhou, J.B., and Wang, F., 2012, Temperature, Pressure, and Composition of the Mantle Source Region of Late Cenozoic Basalts in Hainan Island, SE Asia: a Consequence of a Young Thermal Mantle Plume close to Subduction Zones?: Journal of Petrology, v. 53, no. 1, p. 177−233.

Willbold, M., and Stracke, A., 2006, Trace element composition of mantle end-members: Implications for recycling of oceanic and upper and lower continental crust: Geochemistry Geophysics Geosystems, v. 7, Q04004.

Winchester, J. A., and Floyd, P. A., 1977, Geochemical discrimination of different magma series and their differentiation products using immobile elements: Chemical Geology, v. 20, no. 4, p. 325-343.

Workman, R. K., Hauri, E., Hart, S. R., Wang, J., and Blusztajn, J., 2006, Volatile and trace elements in basaltic glasses from Samoa: Implications for water distribution in the mantle: Earth and Planetary Science Letters, v. 241, no. 3–4, p. 932–951.

Xu, J.F., and Castillo, P.R., 2004, Geochemical and Nd–Pb isotopic characteristics of the Tethyan asthenosphere: implications for the origin of the Indian Ocean mantle domain: Tectonophysics, v. 393, p. 9-27.

Yang, Y.H., Wu, F.Y., Yang, J.H., Chew, D. M., Xie, L.W., Chu, Z.Y., Zhang, Y.B., and Huang, C., 2014, Sr and Nd isotopic compositions of apatite reference materials used in U–Th–Pb geochronology: Chemical Geology, v. 385, p. 35-55.

Zeng, L.S., Gao, L.E., Xie, K.J., and Jing, L.Z., 2011, Mid-Eocene high Sr/Y granites in the Northern Himalayan Gneiss Domes: Melting thickened lower continental crust: Earth and Planetary Science Letters, v. 303, p. 251–266.

Zhang, H., Harris, N., Parrish, R., Kelley, S., Zhang, L., Rogers, N., Argles, T., and King, J., 2004, Causes and consequences of protracted melting of the mid-crust exposed in the North Himalayan antiform: Earth and Planetary Science Letters, v. 228, p. 195–212.

Table DR1. **Titanite SIMS U-Pb data for Langshan mafic rock**

Spot number	U (ppm)	Th/U	$^{238}U/^{206}Pb$	±σ (%)	$^{207}Pb/^{206}Pb$	±σ (%)	207-corr age (Ma)	±σ (Ma)
13JT04@01	3.2	1.42	1.54	1.5	0.81	0.6	124	514
13JT04@02	9.7	0.04	61.15	3.6	0.51	2.6	43	8
13JT04@03	5.9	2.70	1.38	1.9	0.80	0.4	152	566
13JT04@04	3.4	0.23	16.06	10.5	0.74	1.8	46	46
13JT04@05	7.1	1.20	3.30	3.4	0.80	0.5	85	236
13JT04@06	4.7	0.72	1.75	2.2	0.81	0.4	75	458
13JT04@07	16.9	0.09	24.50	3.5	0.69	1.1	46	28
13JT04@08	2.7	0.09	41.23	2.5	0.60	3.9	46	15
13JT04@09	2.5	0.20	10.09	2.1	0.78	1.4	38	77
13JT04@10	2.9	2.07	2.07	1.5	0.83	0.6	17	395
13JT04@11	8.8	0.14	44.07	1.6	0.58	1.7	47	13
13JT04@12	2.2	0.07	1.54	1.5	0.82	0.6	76	521
13JT04@13	10.1	0.12	16.37	1.5	0.75	0.8	38	45
13JT04@14	17.8	0.62	3.64	1.5	0.80	0.3	76	214
13JT04@15	22.3	0.20	3.95	1.6	0.79	0.3	80	196
13JT04@16	2.9	0.22	1.79	3.3	0.83	0.7	~~-12~~	~~462~~
13JT04@17	5.2	0.11	33.44	1.6	0.63	1.7	48	18
13JT04@18	7.1	0.54	1.37	1.5	0.81	0.3	125	578
13JT04@19	3.6	1.98	0.57	1.5	0.81	0.3	263	1381
13JT04@20	5.6	0.27	3.85	2.1	0.78	0.8	97	200
13JT04@21	6.1	0.92	1.15	1.8	0.82	0.6	62	706
13JT04@22	3.9	0.09	3.33	1.5	0.81	0.6	44	240
13JT04@23	1.4	0.39	1.61	1.5	0.80	0.7	132	486
13JT04@24	14.8	0.50	1.76	2.2	0.81	0.2	96	452
13JT04@25	8.9	0.12	45.47	2.4	0.54	1.8	53	11
13JT04@26	12.3	0.76	3.91	1.5	0.80	0.4	69	200
13JT04@27	3.4	0.44	11.12	1.5	0.75	1.2	57	67
13JT04@28	7.2	0.15	16.67	1.7	0.74	0.9	46	43
13JT04@29	13.1	0.06	40.44	1.7	0.61	1.3	44	15
13JT04@30	7.4	0.07	2.59	1.5	0.81	0.5	48	310
13JT04@31	8.1	0.09	12.19	2.2	0.77	0.9	41	62
13JT04@32	8.5	0.17	29.69	1.5	0.66	1.5	47	22
13JT04@33	2.7	3.10	0.76	1.6	0.80	0.8	275	1022
13JT04@34	18.1	1.27	3.59	1.6	0.79	0.3	85	216
13JT04@35	12.8	0.04	65.03	1.6	0.48	1.7	45	7
13JT04@36	10.3	0.49	2.63	1.5	0.80	0.3	88	298
13JT04@37	5.0	1.78	0.61	1.5	0.82	0.4	126	1315
13JT04@38	2.4	0.30	42.65	5.4	0.59	2.8	46	14
13JT04@39	3.7	0.22	8.57	1.5	0.78	1.0	45	90
13JT04@40	7.5	0.15	2.46	2.2	0.81	0.7	71	323
13JT04@41	5.9	0.21	3.46	1.5	0.81	0.6	37	232

13JT04@42	5.0	0.11	3.55	1.5	0.81	0.5	36	226
13JT04@43	2.5	0.36	7.09	2.4	0.79	1.0	45	110
13JT04@44	4.1	0.51	9.09	1.7	0.76	1.3	60	83
13JT04@45	3.5	1.91	0.60	1.5	0.81	0.4	332	1296
13JT04@46	4.4	0.10	33.65	3.9	0.64	2.0	47	19
13JT04@47	4.1	0.23	1.53	1.5	0.82	0.4	64	525
13JT04@48	25.7	0.09	11.26	1.5	0.76	0.5	53	66
13JT04@49	7.2	0.94	1.52	1.5	0.81	0.4	92	523

Table DR2. Whole-rock geochemical data

Sample	12FW58	12FW61	12FW63	13JT04	13JT05	13JT06
Major element (wt.%)						
SiO_2	43.92	46.37	42.25	42.66	44.49	44.56
TiO_2	3.09	2.99	3.56	2.97	2.85	3.02
Al_2O_3	12.97	16.96	16.22	14.41	14.19	14.58
TFeO	11.42	9.92	11.11	9.98	8.35	8.76
MnO	0.19	0.13	0.13	0.15	0.13	0.13
MgO	9.70	4.03	6.61	7.03	7.36	7.34
CaO	8.50	6.25	6.77	7.78	11.09	10.79
Na_2O	2.95	5.88	3.56	4.03	3.67	3.71
K_2O	0.08	0.33	0.78	0.15	0.17	0.25
P_2O_5	0.61	0.72	0.42	0.49	0.35	0.44
H_2O^+	4.93	3.56	5.09	4.75	3.75	3.68
CO_2	2.42	4.03	4.76	5.31	2.53	1.65
LOI	6.21	6.59	8.65	9.26	5.92	4.93
Normalized to 100% on the basis of volatile-free (wt.%)						
SiO_2	47.00	49.55	46.22	47.59	48.02	47.61
TiO_2	3.31	3.19	3.89	3.31	3.08	3.23
Al_2O_3	13.89	18.12	17.75	16.07	15.32	15.58
TFeO	12.23	10.60	12.15	11.13	9.01	9.36
MnO	0.20	0.14	0.14	0.17	0.14	0.14
MgO	10.38	4.31	7.23	7.84	7.94	7.84
CaO	9.09	6.68	7.41	8.68	11.97	11.53
Na_2O	3.16	6.28	3.89	4.50	3.96	3.96
K_2O	0.08	0.35	0.85	0.17	0.18	0.27
P_2O_5	0.66	0.77	0.46	0.55	0.37	0.47
Trace element (ppm)						
V	206	151	294	275	298	314
Cr	222	3	10	40	220	210
Mn	1399	1002	947	1162	1007	1007
Co	47	27	48	36	35	38
Ni	172	9	45	45	69	73
Cu	49	48	85	69	68	69
Zn	114	93	103	92	70	77
Ga	21	22	20	20	18	19
Rb	4.2	12	28	3.6	4.3	6.2
Sr	582	697	389	635	843	592
Y	30.9	34.3	24.4	26.4	24.8	27.5
Zr	289	224	170	172	157	171
Nb	70	87	52	47	36	39
Cs	1.78	0.5	0.81	0.81	0.62	0.55
Ba	453	556	326	284	739	1450
La	43.3	41.1	25.8	27.2	21.8	25.0
Ce	87.2	81.0	49.7	55.6	45.2	51.5

Pr	10.81	9.93	6.21	6.78	5.70	6.33
Nd	43.1	39.7	25.0	29.5	25.4	29.6
Sm	9.06	8.89	5.80	6.62	6.00	6.96
Eu	2.97	2.70	1.96	2.44	2.17	2.54
Gd	8.05	8.19	5.62	6.76	6.47	7.33
Tb	1.15	1.19	0.85	1.01	0.97	1.07
Dy	6.20	6.65	4.84	5.47	5.43	5.82
Ho	1.13	1.28	0.93	1.03	0.95	1.04
Er	2.73	3.13	2.26	2.67	2.47	2.68
Tm	0.36	0.42	0.31	0.32	0.30	0.33
Yb	2.15	2.56	1.86	1.86	1.68	1.88
Lu	0.29	0.36	0.25	0.27	0.23	0.26
Hf	6.4	4.4	3.8	4.4	4.4	4.7
Ta	4.4	4.8	3.0	2.5	1.9	2.2
Pb	3.1	2.4	2.4	1.8	1.4	1.6
Th	5.92	5.68	3.76	3.48	2.84	3.22
U	1.48	1.32	0.91	0.90	0.69	0.78
Sr-Nd isotopes						
$^{87}Sr/^{86}Sr$	0.706739	0.706738	0.706719	0.707161	0.707302	0.707120
2SE	0.000014	0.000013	0.000014	0.000013	0.000014	0.000014
$^{87}Sr/^{86}Sr(t)$	0.706726	0.706705	0.706584	0.707151	0.707293	0.707101
$^{143}Nd/^{144}Nd$	0.512878	0.512896	0.512917	0.512918	0.512935	0.512937
2SE	0.000003	0.000004	0.000004	0.000004	0.000003	0.000004
$\varepsilon_{Nd}(0)$	4.7	5.0	5.4	5.5	5.8	5.8
$\varepsilon_{Nd}(t)$	5.1	5.4	5.8	5.8	6.1	6.1
$f_{Sm/Nd}$	-0.35	-0.31	-0.29	-0.31	-0.27	-0.28

263

Table DR3. **Apatite Sr isotopic data**

Sample	$^{87}Rb/^{86}Sr$	2σ	$^{87}Sr/^{86}Sr$	2σ	Age (Ma)	$^{87}Sr/^{86}Sr(t)$	2σ
12FW63: $^{87}Sr/^{86}Sr(t)$ = 0.70317±0.00006 (MSWD=2.3, n=24)							
12FW63 01	0.00059	0.00006	0.70327	0.00013	45	0.70327	0.00013
12FW63 02	0.00077	0.00009	0.70318	0.00019	45	0.70318	0.00019
12FW63 03	0.00047	0.00006	0.70328	0.00016	45	0.70328	0.00016
12FW63 04	0.00076	0.00011	0.70324	0.00024	45	0.70324	0.00024
12FW63 05	0.00121	0.00017	0.70338	0.00019	45	0.70338	0.00019
12FW63 06	0.00075	0.00010	0.70319	0.00016	45	0.70319	0.00016
12FW63 07	0.00140	0.00027	0.70320	0.00023	45	0.70320	0.00023
12FW63 08	0.00134	0.00010	0.70338	0.00021	45	0.70338	0.00021
12FW63 09	0.00058	0.00006	0.70298	0.00016	45	0.70298	0.00016
12FW63 10	0.00121	0.00029	0.70334	0.00044	45	0.70334	0.00044
12FW63 11	0.00043	0.00006	0.70304	0.00014	45	0.70303	0.00014
12FW63 12	0.00095	0.00007	0.70316	0.00016	45	0.70316	0.00016
12FW63 13	0.00149	0.00025	0.70321	0.00017	45	0.70321	0.00017
12FW63 14	0.00174	0.00035	0.70293	0.00033	45	0.70292	0.00033
12FW63 15	0.00294	0.00053	0.70288	0.00017	45	0.70288	0.00017
12FW63 16	0.00125	0.00012	0.70314	0.00016	45	0.70314	0.00016
12FW63 17	0.00095	0.00009	0.70320	0.00014	45	0.70320	0.00014
12FW63 18	0.00084	0.00018	0.70337	0.00020	45	0.70337	0.00020
12FW63 19	0.00106	0.00022	0.70324	0.00019	45	0.70324	0.00019
12FW63 20	0.00052	0.00004	0.70315	0.00018	45	0.70315	0.00018
12FW63 21	0.00092	0.00007	0.70304	0.00021	45	0.70304	0.00021
12FW63 22	0.00035	0.00005	0.70329	0.00019	45	0.70329	0.00019
12FW63 23	0.00080	0.00019	0.70292	0.00019	45	0.70292	0.00019
12FW63 24	0.00056	0.00007	0.70304	0.00023	45	0.70304	0.00023
13JT04: $^{87}Sr/^{86}Sr(t)$ = 0.70312±0.00004 (MSWD=2.2, n=29)							
13JT04 01	0.00026	0.00003	0.70323	0.00018	45	0.70323	0.00018
13JT04 02	0.00028	0.00002	0.70320	0.00016	45	0.70320	0.00016
13JT04 03	0.00032	0.00003	0.70309	0.00016	45	0.70309	0.00016
13JT04 04	0.00032	0.00002	0.70339	0.00012	45	0.70339	0.00012
13JT04 05	0.00024	0.00002	0.70292	0.00016	45	0.70292	0.00016
13JT04 06	0.00026	0.00002	0.70322	0.00015	45	0.70322	0.00015
13JT04 07	0.00029	0.00002	0.70304	0.00013	45	0.70304	0.00013
13JT04 08	0.00118	0.00020	0.70327	0.00016	45	0.70327	0.00016
13JT04 09	0.00068	0.00010	0.70297	0.00014	45	0.70297	0.00014
13JT04 10	0.00032	0.00005	0.70301	0.00017	45	0.70301	0.00017
13JT04 11	0.00034	0.00003	0.70322	0.00017	45	0.70322	0.00017
13JT04 12	0.00025	0.00002	0.70299	0.00015	45	0.70299	0.00015
13JT04 13	0.00050	0.00014	0.70315	0.00015	45	0.70315	0.00015
13JT04 14	0.00044	0.00002	0.70317	0.00013	45	0.70317	0.00013
13JT04 15	0.00040	0.00005	0.70314	0.00019	45	0.70314	0.00019

13JT04 16	0.00060	0.00010	0.70321	0.00017	45	0.70321	0.00017
13JT04 17	0.00023	0.00002	0.70306	0.00015	45	0.70306	0.00015
13JT04 18	0.00024	0.00002	0.70307	0.00013	45	0.70307	0.00013
13JT04 19	0.00126	0.00019	0.70306	0.00017	45	0.70306	0.00017
13JT04 20	0.00027	0.00002	0.70300	0.00012	45	0.70300	0.00012
13JT04 21	0.00033	0.00005	0.70309	0.00019	45	0.70308	0.00019
13JT04 22	0.00026	0.00003	0.70310	0.00017	45	0.70310	0.00017
13JT04 23	0.00036	0.00010	0.70307	0.00015	45	0.70307	0.00015
13JT04 24	0.00025	0.00002	0.70299	0.00014	45	0.70299	0.00014
13JT04 25	0.00065	0.00014	0.70312	0.00030	45	0.70312	0.00030
13JT04 26	0.00035	0.00005	0.70332	0.00018	45	0.70332	0.00018
13JT04 27	0.00031	0.00003	0.70314	0.00017	45	0.70314	0.00017
13JT04 28	0.00039	0.00006	0.70312	0.00016	45	0.70312	0.00016
13JT04 29	0.00032	0.00003	0.70316	0.00017	45	0.70316	0.00017

264

Table DR4. **Apatite Nd isotopic data**

Sample	$^{147}Sm/^{144}Nd$	2σ	$^{143}Nd/^{144}Nd$	2σ	T(Ma)	$^{143}Nd/^{144}Nd(t)$	$\varepsilon_{Nd}(0)$	$\varepsilon_{Nd}(t)$	2σ
12FW60: $\varepsilon_{Nd}(t)$ = 4.9±0.4 (MSWD=2.4, n=20)									
12FW60 01	0.1223	0.0007	0.51284	0.00005	45	0.51281	4.0	**4.4**	1.0
12FW60 02	0.1270	0.0004	0.51289	0.00005	45	0.51285	4.8	**5.2**	1.0
12FW60 03	0.1211	0.0007	0.51289	0.00005	45	0.51285	4.8	**5.3**	0.9
12FW60 04	0.1216	0.0004	0.51281	0.00006	45	0.51278	3.4	**3.8**	1.3
12FW60 05	0.1251	0.0003	0.51283	0.00005	45	0.51279	3.7	**4.1**	0.9
12FW60 06	0.1288	0.0002	0.51286	0.00006	45	0.51283	4.4	**4.8**	1.1
12FW60 07	0.1235	0.0005	0.51291	0.00005	45	0.51287	5.3	**5.7**	1.0
12FW60 08	0.1265	0.0004	0.51292	0.00006	45	0.51289	5.6	**6.0**	1.2
12FW60 09	0.1262	0.0003	0.51282	0.00006	45	0.51279	3.6	**4.0**	1.2
12FW60 10	0.1196	0.0004	0.51287	0.00005	45	0.51284	4.6	**5.0**	0.9
12FW60 11	0.1236	0.0006	0.51286	0.00005	45	0.51282	4.3	**4.7**	1.0
12FW60 12	0.1297	0.0004	0.51283	0.00006	45	0.51279	3.8	**4.1**	1.1
12FW60 13	0.1284	0.0002	0.51282	0.00006	45	0.51278	3.5	**3.9**	1.3
12FW60 14	0.1266	0.0004	0.51286	0.00006	45	0.51283	4.4	**4.8**	1.1
12FW60 15	0.1261	0.0004	0.51287	0.00006	45	0.51283	4.4	**4.8**	1.1
12FW60 16	0.1242	0.0003	0.51293	0.00005	45	0.51289	5.6	**6.0**	1.0
12FW60 17	0.1213	0.0006	0.51280	0.00005	45	0.51277	3.2	**3.6**	1.0
12FW60 18	0.1280	0.0005	0.51295	0.00005	45	0.51292	6.2	**6.6**	1.0
12FW60 19	0.1245	0.0002	0.51289	0.00006	45	0.51285	4.9	**5.3**	1.1
12FW60 20	0.1290	0.0003	0.51288	0.00006	45	0.51284	4.7	**5.1**	1.2
12FW63: $\varepsilon_{Nd}(t)$ = 5.0±0.4 (MSWD=1.8, n=20)									
12FW63 01	0.1284	0.0002	0.51289	0.00006	45	0.51285	4.9	**5.3**	1.1
12FW63 02	0.1297	0.0002	0.51281	0.00006	45	0.51277	3.3	**3.7**	1.2
12FW63 03	0.1341	0.0001	0.51286	0.00006	45	0.51282	4.3	**4.7**	1.2
12FW63 04	0.1334	0.0001	0.51287	0.00005	45	0.51284	4.6	**5.0**	0.9
12FW63 05	0.1328	0.0003	0.51285	0.00006	45	0.51281	4.1	**4.5**	1.2
12FW63 06	0.1312	0.0004	0.51289	0.00007	45	0.51285	4.9	**5.2**	1.3
12FW63 07	0.1358	0.0003	0.51285	0.00005	45	0.51281	4.1	**4.4**	1.1
12FW63 08	0.1357	0.0003	0.51285	0.00007	45	0.51281	4.1	**4.5**	1.4
12FW63 09	0.1349	0.0002	0.51292	0.00006	45	0.51288	5.5	**5.9**	1.2
12FW63 10	0.1345	0.0002	0.51288	0.00005	45	0.51284	4.7	**5.1**	1.1
12FW63 11	0.1515	0.0008	0.51288	0.00007	45	0.51283	4.7	**5.0**	1.3
12FW63 12	0.1362	0.0002	0.51280	0.00007	45	0.51276	3.1	**3.5**	1.4
12FW63 13	0.1346	0.0001	0.51292	0.00006	45	0.51288	5.5	**5.9**	1.1
12FW63 14	0.1363	0.0002	0.51281	0.00007	45	0.51277	3.4	**3.8**	1.3
12FW63 15	0.1335	0.0002	0.51288	0.00006	45	0.51284	4.6	**5.0**	1.1
12FW63 16	0.1331	0.0002	0.51290	0.00006	45	0.51286	5.2	**5.6**	1.2
12FW63 17	0.1323	0.0003	0.51289	0.00005	45	0.51285	4.9	**5.3**	1.0
12FW63 18	0.1385	0.0007	0.51287	0.00007	45	0.51283	4.6	**4.9**	1.4
12FW63 19	0.1337	0.0002	0.51298	0.00006	45	0.51294	6.7	**7.0**	1.3
12FW63 20	0.1348	0.0002	0.51284	0.00007	45	0.51280	3.9	**4.3**	1.4

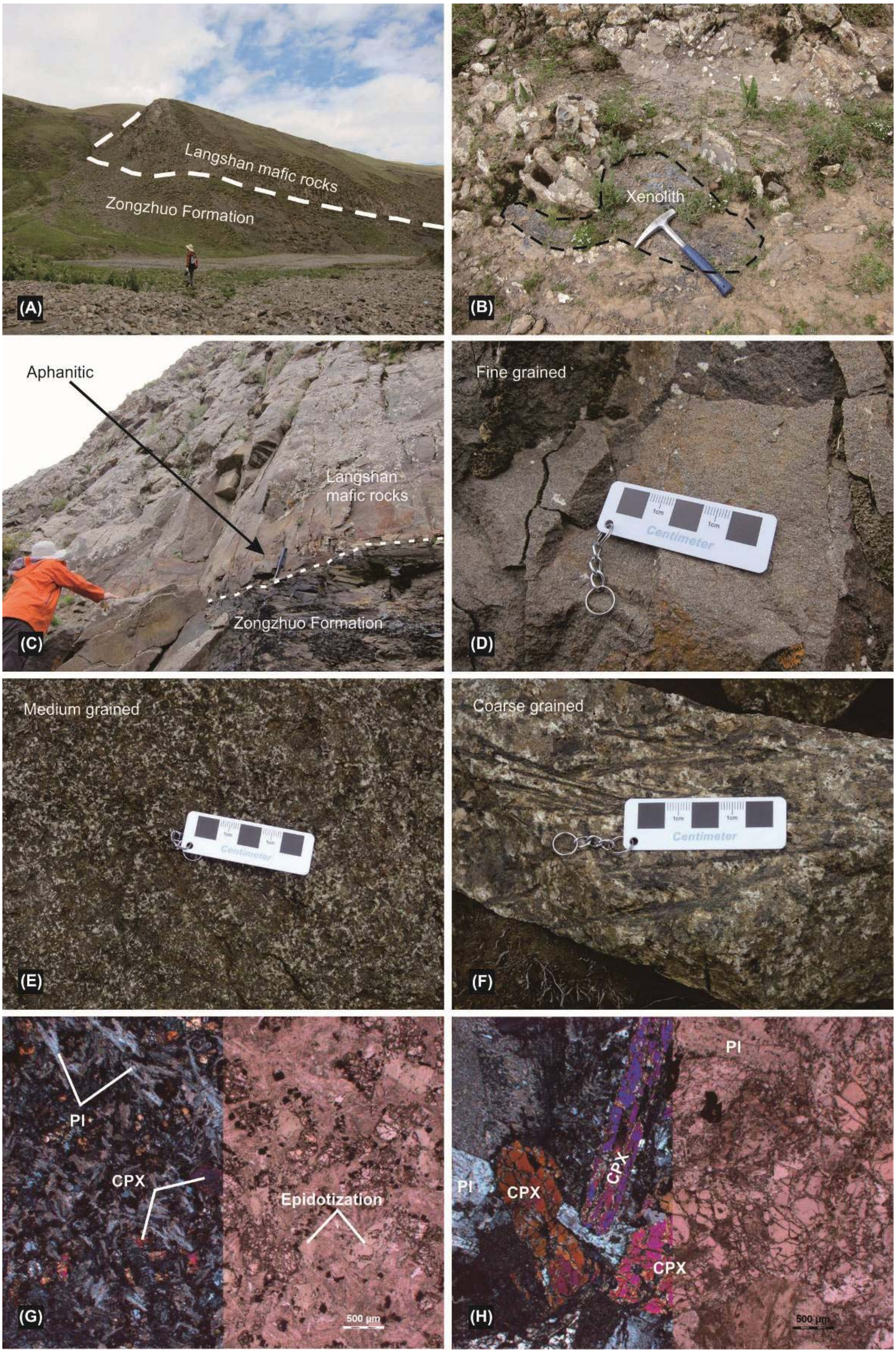

Figure DR1. Pictures of Langshan mafic rocks showing field and petrography characters. (a) Field contact relations with wall rocks. (b) Shale xenolith from wall rock. (c-d) Various textures from aphanitic in the margin to coarse-grained in the central part. (g) and (h) Microphotograph for Samples 12FW58 (fine-grained) and 13JT06 (coarse-grained), respectively.

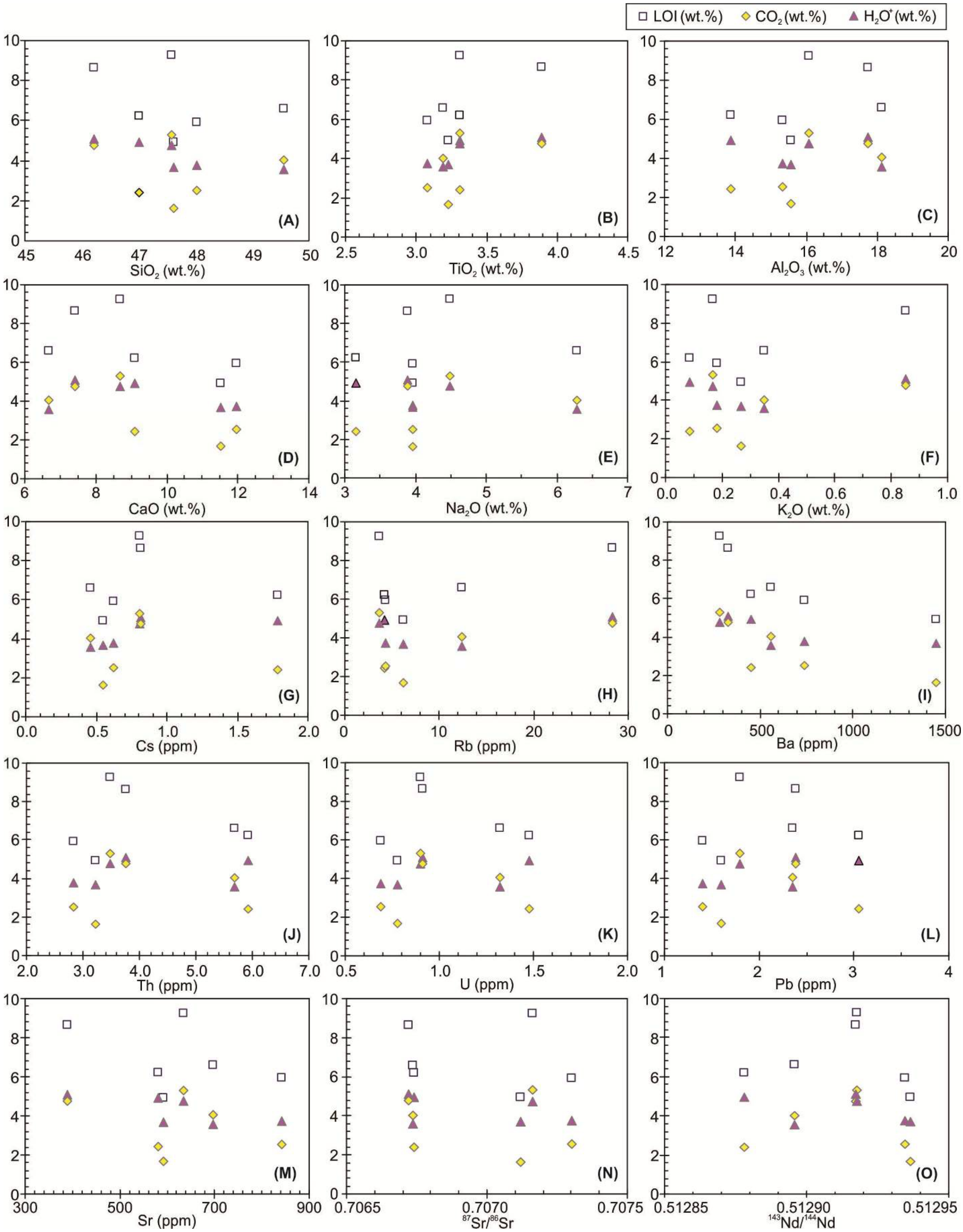

Figure DR2. Variation diagrams showing possible effect of hydrothermal alteration on major elements and fluid-mobile trace elements.

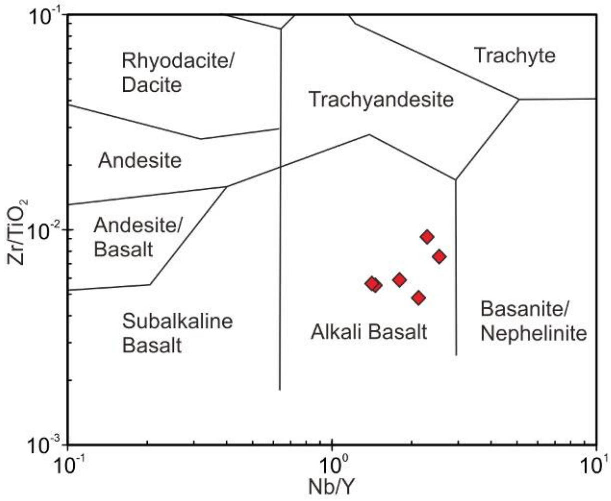

Figure DR3. Nb/Y vs. Zr/TiO_2 diagram for Langshan mafic rocks (Winchester and Floyd, 1977).

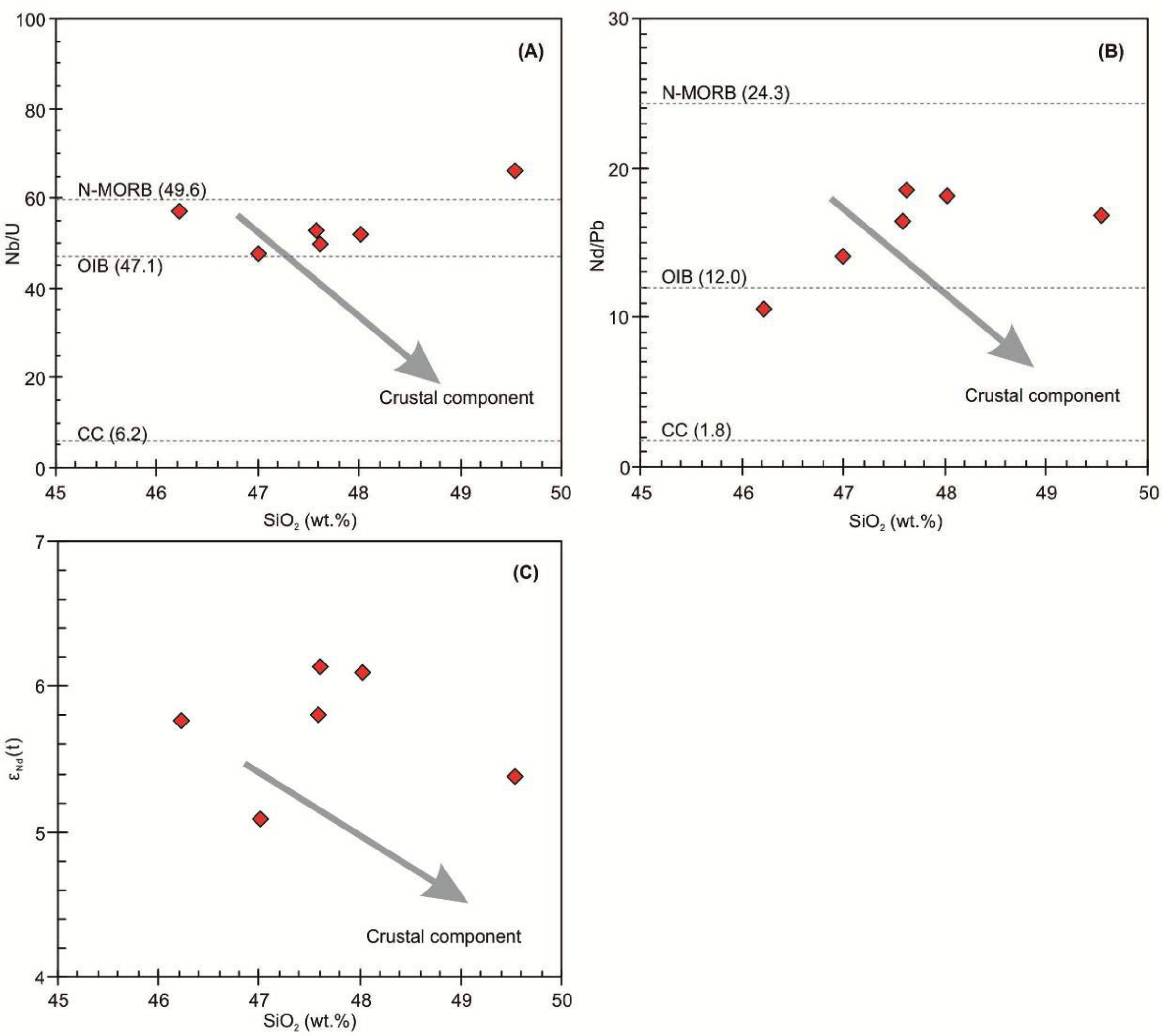

Figure DR4. Plots of Nb/U vs. SiO_2 (a), Nd/Pb vs. SiO_2 (b), and $\varepsilon_{Nd}(t)$ vs. SiO_2 (c). The data for OIB and N-MORB, and CC are from Sun and McDonough (1989) and Rudnick and Gao (2003), respectively.

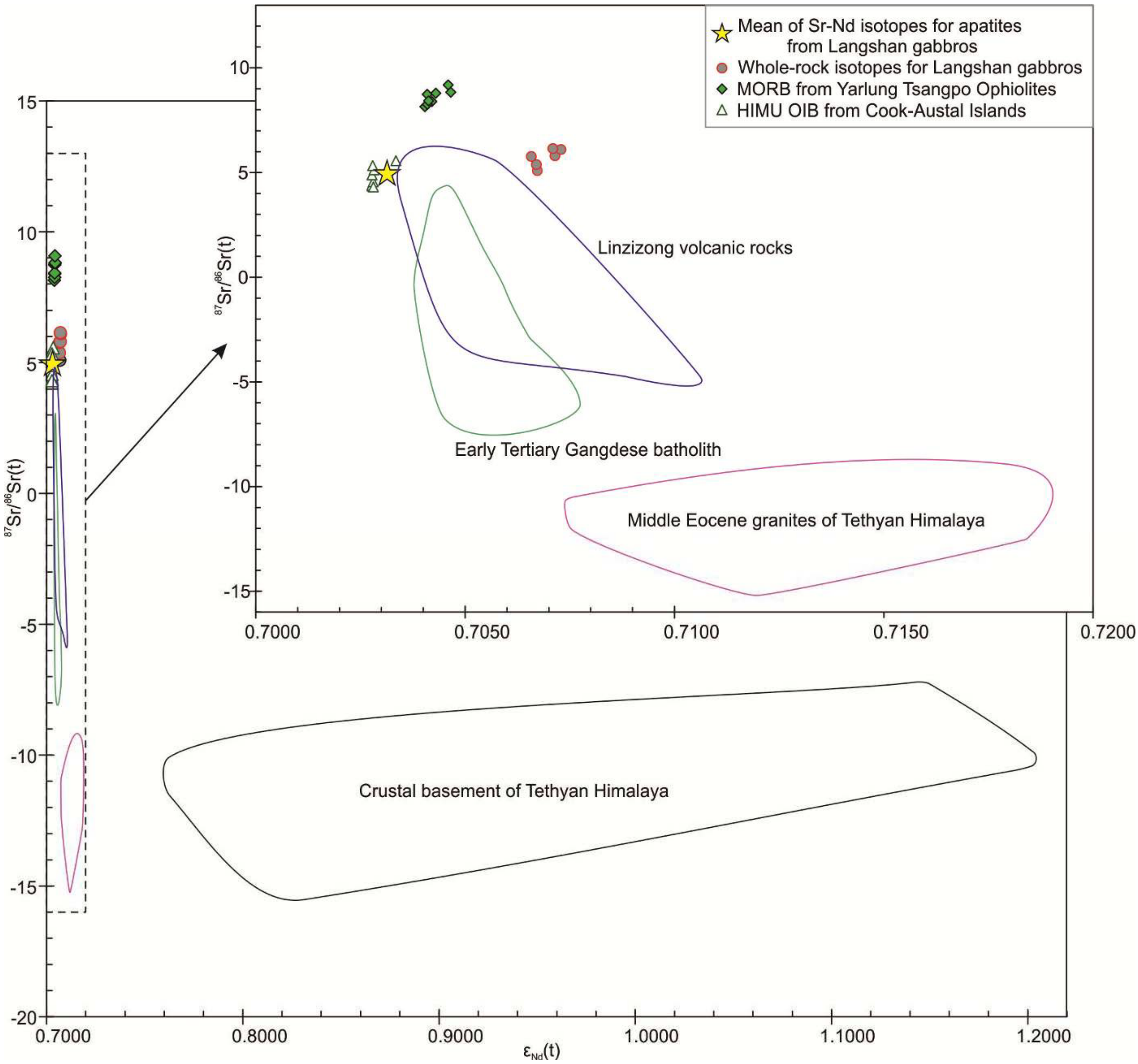

Figure DR5. Sr-Nd isotopic diagram for Langshan gabbros with related data for the early Tertiary magmatism in southern Tibet, the crustal basement of Tethyan Himalaya (gneiss: Zeng et al., 2011; Zhang et al., 2004), MORB from Yarlung Tsangpo Ophiolites (Mahoney et al., 1998; Xu and Castillo, 2004), and HIMU OIB from Cook-Austal Islands (Hanyu et al., 2011) shown for comparison. Other data sources include: middle Eocene granites of Tethyan Himalaya (Aikman et al., 2012; Hou et al., 2012; Liu et al., 2014; Zeng et al., 2011), early Tertiary Gangdese batholith (Jiang et al., 2014; Ma et al., 2014; Wang et al., 2015a, 2015b; and references therein), and Linzizong volcanic rocks (Lee et al., 2012; Mo et al., 2007, 2008). The data for MORB from Yarlung Tsangpo Ophiolites and crustal basement of Tethyan Himalaya were age corrected by 45 Ma. As the apatites are not big enough to be analyzed of Sr and Nd isotopes on one single crystal, we weighted all the apatite Sr and Nd isotopic compositions to represent the Sr-Nd characteristics of Langshan gabbro on the diagram.